

Experimental and numerical investigation of evaporating mono-component droplets in turbulent channel flow

V. Bodoc^{*}, O. Rouzaud^{*}, F. Moreau^{**}, R. Bazile^{**}, and G. Lavergne^{*}

^{*}Département Modèles pour l'Aérodynamique et l'Énergétique, ONERA

2, avenue Eduard Belin, 31055 Toulouse CEDEX 4, France

^{**} Institut de Mécanique des Fluides de Toulouse

Avenue du professeur Camille Soula, 31400 Toulouse, France

Abstract

This paper deals with the experimental investigation and numerical simulation of a cloud of mono-component droplets in a highly turbulent flow. Experimental data and numerical results are compared in order to validate the evaporation models implemented in the computing code. For the liquid phase, the droplets diameter, velocity and temperature are measured at different distances from the atomizer. The diameter and velocity probability functions are recorded in order to have information about the droplets turbulent dispersion and evaporation inside the channel flow. The droplets mean temperature is also measured to evaluate the heat transfer between the two phases.

Introduction

In the combustion of liquid fuels, the droplet vaporization rate is an important factor. Thus, the study of the droplet evaporation in a real turbulent environment is of great importance for different engineering applications as internal combustion engines, gas turbines, rocket engines, industrial burners. The experimental investigation of real combustors is expensive and even impossible to be realized. A solution could be the numerical simulation of the processes involved in the burning of a liquid fuel: atomization, droplets dispersion, wall interaction, droplets evaporation, combustion. To be able to accurately calculate the evaporation of fuels, some evaporation models need to be developed and implemented in the computing codes. Up to now, at ONERA, different evaporation models for mono and multi-component liquids were tested for isolated droplets (researches of N. Doué [1] and C. Laurent [2]). The use of these models furnished very satisfactory results for a monodisperse droplet stream.

In order to get closer to the real combustor, these evaporation models, implemented in the ONERA's CEDRE code, were applied for more complex configurations. In a previous paper, the authors presented experimental and numerical results obtained for a mono-component, polydisperse spray evolving in a quiescent atmosphere [3]. A bi-component liquid was also studied and the results will be soon presented. The comparison of the results showed a good agreement between the experiment and numerical simulation and motivated the investigation of a more complex environment.

Such a configuration, that allows the reproduction of a high turbulent and heated flow, had already been developed at IMFT. For this configuration M.Cochet [4] realized in a first step the characterization of the continuous phase using the Particle Image Velocimetry (PIV) technique. In a second step, the same author investigated the vaporization of an acetone polydisperse droplets using the a Planar Laser Induced Fluorescence (PLIF) system. Later, in order to evaluate the fuels vaporization, V. Bodoc and F. Moreau [5] measured the droplets temperature, size and velocity for mono and bi-component liquids. A part of the experimental database will be used in the present study to be compared to the numerical results.

The main goal of this work is to study by numerical simulation the behavior of evaporating droplets in a highly turbulent channel flow. The liquid dispersed phase is studied in terms of droplet size, velocity and temperature evolutions in the channel. In this paper only the vaporization of the pure n-octane droplets will be explored. The first section reviews the experimental bench and measurement techniques. The second section will be focused on the numerical simulation of the confined spray.

Materials and Methods

Experimental investigation.

The experimental setup consists in a vertical square cross-section channel with optical access (**Figure 1**). Preheated air is injected in a tank and passes through a turbulence generator before entering the channel. The generator is made of a circular plate perforated by 45 holes of 3mm diameter and a convergent. The 45 jets im-

* Virginel BODOC: virginel.bodoc@onera.fr

pinge the convergent generating a high turbulence level. An ultrasound atomizer is placed in the centre of the perforated plate and nozzle tip is located at the entrance of the square section channel. The atomization process provides droplets with a wide range of diameters and velocities.

The measurement methods mounted on the experimental bench are the Global Rainbow Thermometry (GRT) and Phase Doppler Anemometry (PDA). The positioning of the GRT and PDA equipments with respect to the channel flow is described in **Figure 2**. To measure the diameter, axial and radial velocity of each droplet, a commercial PDA is used. The temperature is deduced with the GRT technique. The light source used is a HeNe continuous laser delivering a power of 30mW. The cloud of droplets is submitted to the laser beam. The first lens of the receiving optical system realizes an optical Fourier transformation of the scattered light. In this way, in the focal plane of the first lens, the light intensity is expressed only as a function of the scattering angle and is independent of the droplet position in the probe volume. The image of the optical Fourier transformation is reproduced by the second lens on the CCD linear sensor. A diaphragm disposed in the image plane of the first lens can be used to control the dimension of the probe volume. Before starting measurements, a relation between the scattering angle and the corresponding pixel on the CCD sensor has to be found. This task was achieved by the use of a mirror disposed in the probe volume.

The time of the acquisition is determined by the exposure time of the CCD camera. This is controlled such that a great number of droplets crosses the probe volume. In regions with a reduced density of droplets the exposure time had to be increased accordingly. The signal is transferred to a computer via an acquisition board.

Once the optical signal is recorded, a software application, developed at the CORIA laboratories, is used to estimate the mean refractive index of all the droplets crossing the probe volume. This code is based on an inversion algorithm that uses the Complex Angular Momentum Theory (CAMT) of Nussenzveig to estimate the scattered light intensity as a function of the droplet diameter and the refractive index. The minimization of the differences between the recorded and computed signal is done by the nonnegative least square (NNLS) method [6]. Since GRT provides only the refractive index of the droplets, a correlation between the refractive index and the liquid temperature needs to be determined. This correlation is obtained by using a multi spectral refractometer available at laboratory.

The operating conditions are detailed in the **Table 1**.

Numerical method

In the second part of the paper the results of a Large Eddy Simulation (LES) of this multiphase flow are presented. The governing equations were solved using the computing code CEDRE developed at ONERA. The LES simulation is performed to investigate the temporal and spatial evolution of the confined turbulent flow. The properties of the turbulence in the square cross section channel are studied by analyzing the temporal evolution of the flow field. The simulation results are compared with experimental data.

Problem definition

The geometry used in the numerical simulation is identical to the experimental configuration and is presented in the **Figure 3**. In the picture the position of injection points and the velocity vectors are represented. As it is very difficult to measure the values at the entrance in the square section channel, the flow in the convergent needs to be considered. Nevertheless, because of the high complexity of the flow structure, the numerical simulation of this region is not easy. The generation of vortices near the entrance holes, the entrainment of fluid from the surrounding medium, the oblique impingement of jets, the effects of the confining walls, the separation of flow, are factors that contribute to the complexity of the problem. These mechanisms were experimentally demonstrated by Özdemir and Whitelaw in 1992 [7]. The complexity of the problem and the strong anisotropy of the flow at least in the convergent and in the first part of the channel justify the use of LES approach.

For an efficient and accurate calculation of the turbulent flow in the channel, a dense mesh is realized. The number of cells exceeds 6 millions. The mesh is more refined in the region of free jets and jets impacting the convergent in anticipation of resolving the regions with high turbulence energy production. Previous DNS and LES calculations of the square duct flow indicate that a maximum grid spacing of about $x^+ \leq 2$ is needed in the direction perpendicular to wall to resolve the flow near a corner [8]. In the current simulation the grid resolution near the corner is: $0.9 < x^+ < 5$. Concerning the numerical simulation with a LES approach of the jets impinging a surface, Y.M. Chung et al [9] realized a numerical study in order to estimate the momentum and heat transfer characteristics of an unsteady impinging jet on a plate. For a non-dimensional length of the jet $L/D_j = 10$ and a Reynolds number $Re=1000$ (based on the jet initial width D_j) they used 384 computational points. In reference to this work, in the present paper, for a Reynolds number $Re=3500$ and a non-dimensional length of the jet $L/D_j = 7$, 60 computational points were used. The number of the computational points is limited by the physical limits of the computing machine.

A 10^{-5} s constant time step is used during the calculations and corresponds to a maximum CFL value of 6. The initial condition is set as a uniform flow. The grid is constructed such that it can resolve the large eddies.

The smaller eddies, supposed to be isotropic, are modeled by a subgrid scale model. For this simulation, a standard Smagorinsky model is used. The equations are integrated in time using an implicit, second-order accurate Runge-Kutta method.

Dispersed phase equations.

A two-way coupling computation of the spray is performed through an Eulerian-Lagrangian approach. The discrete phase is solved by a Lagrangian tracking methodology. Each particle and, in particular, the smallest ones, are sensitive to the structures in the flow. The main advantage of this methodology is that it allows a detailed study of the droplets displacement in the carrier flow. The unsteady technique used in the numerical computation consists in the following of a large number of numerical droplets representing real droplets with close properties: position, radius, velocity, temperature. Various effects as droplet collision, break-up and coalescence are neglected in reason of the small liquid volume fractions.

The Lagrangian motion of a rigid, spherical droplet in a flow is governed by a force balance equation. Forces acting on the droplets are assumed to be the drag force and the gravity. Any other forces which can act on the droplet are neglected, assuming that there is no loss of accuracy.

The droplet equations of motions are given in the following. The next equation characterizes each droplet:

$$dx_p = v_p \cdot dt \quad (1)$$

The force balance equation is of the form:

$$dv_p = \frac{U_g - v_p}{\tau_p} \cdot dt + g \cdot dt \quad (2)$$

The first term in the right hand side represents the drag force. The drag force is taken into account by the means of the dynamic relaxation time τ_p . The Shiller & Neuman correlation is used to relate the droplet drag coefficient to the droplet vaporization:

$$Cd = \begin{cases} \frac{24}{Re_p} \cdot (1 + 0.15 \cdot Re_p^{0.687}) & \text{if } Re_p \leq 1000 \\ 0.445 & \text{if } Re_p \geq 1000 \end{cases} \quad (3)$$

where Re_p stands for the droplet Reynolds number. The second term in the right hand side of the equation (2) represents the gravity force.

As evaporation modifies droplet size, equation (4) is used to predict droplet diameter evolution.

$$\frac{d(r_p)^2}{dt} = - \frac{\mu_g \cdot Sh}{\rho_p \cdot Sc} \cdot \ln(1 + B_M) \quad (4)$$

Convection influence on the evaporation rate is taken into account by the use of the Ranz-Marshall model for the Sherwood number:

$$Sh = 2 + 0.57 \cdot Re_p^{1/2} \cdot Sc_p^{1/3} \quad (5)$$

The temperature evolution is evaluated using the next equation:

$$m_p c_{pl} \frac{dT_p}{dt} = 2\pi \cdot Nu \cdot \lambda_g \cdot r_p \cdot (T_g - T_p) \cdot \frac{\ln(1 + B_T)}{B_T} - \frac{dm_p}{dt} \cdot L_v(T_p) \quad (6)$$

The droplet cooling is calculated with the Ranz-Marshall assumption for the Nusselt number:

$$Nu = 2 + 0.57 \cdot Re_p^{1/2} \cdot Pr^{1/3} \quad (7)$$

Average thermophysical properties near the droplet surface are obtained with the 1/3 rule.

Injection modelling.

A special attention was paid to droplet injection. The Lagrangian approach used in this simulation needs as input data the initial characteristics of the droplets as: temperature, size and velocity. To perform the injection of the droplets for the confined flow, the experimental data base obtained for a non-confined spray will be used. This is possible because the same liquids are used in both configurations and parameters like flow rate, ampli-

tude and excitation frequency for the ultrasonic atomizer are equal in both cases. The results obtained at 10 mm from the nozzle tip are used to generate the numerical droplets. In this region it can be supposed that the primary atomization process is completed and spherical droplets are formed. Also, it is assumed that the turbulent flow do not change essentially the spray behavior at 10 mm from the injector tip. Moreover, the mean evolution of the spray allows to assume an axial symmetry.

The PDA technique provided the droplets sizes and velocity, while the GRT technique the droplets temperature. The purpose is to model the droplet injection by a conical spray. This representation is realized by a distribution of a number of injector points in a section. This section is the same with the one used for experimental measurements. The assumption of axial symmetry of the spray allows the repartition of the injection points onto different concentric circles as in **Figure 4**. Because the size distribution has a radial evolution within the spray (

Figure 5 and **Figure 6**), the same distribution is assumed for all injection points disposed on each circle. Furthermore, every real distribution is described by 5 numerical classes and the decomposition technique is explained throughout **Figure 6**.

For every distribution i and class j , the mean diameter is computed with the expression:

$$D_{i,j} = \frac{\sum_{q=1}^{N_{c,i,j}} n_q \cdot D_q}{\sum_{q=1}^{N_{c,i,j}} n_q}, \quad (8)$$

where $N_{c,i,j}$ represents the number of experimental classes corresponding to the distribution i and numerical class j . Analogically, the mean velocity is computed with the equation:

$$v_{i,j} = \frac{\sum_{q=1}^{N_{c,i,j}} n_q \cdot v_q \cdot D_q^3}{\sum_{q=1}^{N_{c,i,j}} n_q \cdot D_q^3} \quad (9)$$

A mass flow rate has also to be estimated for every distribution i and class j . The calculation is performed with the equation:

$$\dot{m}_{i,j} = \alpha_{i,j} \cdot \dot{m}_l \quad (10)$$

where \dot{m}_l represents the total liquid mass flow. The coefficients $\alpha_{i,j}$ are calculated from the mass flow rates provided by the PDA for every distribution $\dot{m}_{PDA,i}$ and size distributions:

$$\alpha_{i,j} = \frac{\dot{m}_{PDA,i} \sum_{q=1}^{N_{c,i,j}} n_q \cdot D_q^3}{\dot{m}_l \sum_{q=1}^{50} n_q \cdot D_q^3} \quad (11)$$

To resume, a number of 640 injection points, distributed on four concentric circles is used.

Discussion of results.

Spatial LES of the continuous phase.

Simulations are firstly performed for the continuous phase without droplets. Once the transient phase is over, temporal averages are computed. To get the mean flow field and turbulence statistics, the flow information is collected over approximately 2 residence time of the flow in the channel. **Figure 7** and **Figure 8** present the radial evolution of the longitudinal mean velocity for two different sections of the channel. The air flow was previously experimentally characterized using LDA with small oil droplets as tracers [4]. At 55 from the entrance in the channel the discrepancies between the experimental and numerical results are important, while at 275 mm the results are identical. **Figure 9** confirms that, axially, downstream in the channel, the tendency is to obtain the same values for experimental and numerical longitudinal mean velocity. Even though there are discrepancies

between the two sets of values, the axial evolution of the mean longitudinal velocity shows a qualitative agreement with the experiment. The numerical velocity profile shown in **Figure 7** seems to correspond more to a “laminar” shape. This aspect makes us believe that, numerically, the turbulence level is inferior to the experiment. The comparison of experimental and numerical turbulent intensities from **Figure 10** confirms this assumption. The discrepancies can be explained by a coarse grid in the region where the turbulence is produced. A detailed presentation of the results of the gaseous flow will be done in another paper. Although the experimental and numerical results obtained for the continuous phase do not quantitatively fully agree, their qualitative correlation allows us to proceed with the multi-phase simulation.

Spatial LES of the multiphase flow.

In a second step, the liquid phase is injected and the influence of the turbulent flow on droplet dispersion and evaporation is observed and compared with experimental data.

The axial evolution of the droplet mean temperature for every class of sizes is presented in **Figure 11**. The heating of droplets is obvious along the channel axis. As it was expected, the droplets with a small diameter heat faster than larger droplets. A comparison of experimental and numerical values shows a qualitative agreement. However, in the first part of the channel, the experimental values are closer to the numerical values corresponding to the largest droplets (class C5). An explanation of these discrepancies can be given by the experimental measurement technique. It is possible that, the small droplets, in reason of their size, do not diffuse enough light in the region of the rainbow angle. Thus, the small droplets “cannot be seen” by the CCD sensor. Only the light diffused by the big droplets contributes to the formation of the global rainbow optical signal. To resume, the temperature measured with the GRT technique is expected to correspond to the temperature of large droplets. **Figure 12** presents the axial evolution of the mean diameter D_{10} for every class of sizes. The evaporation of droplets is clear because the diameter decreases along the channel axis for all classes. Moreover, the droplets from the first class C1 evaporate completely in the first 100 mm from the entrance in the channel, while the class C2 evaporates completely at about 240 mm. A direct result of the disappearance of these classes is the increase of the global mean diameter D_{10} . Qualitatively, the same result is obtained experimentally using the PDA system.

Radial evolutions of the droplet properties were recorded in different sections from the injector. Radial evolutions of the droplet mean temperatures are plotted in **Figure 13-Figure 16**. Note the existence of a temperature radial gradient that is more evident closer to the injector. At short distances from the nozzle tip the spray expansion is fairly narrow and the droplets are not yet fully dispersed by the continuous phase. Thus, the heat exchange is more important at the borders of the spray. Also, it can be seen that small droplets heat more and faster than the largest ones. Further downstream, the temperature tends to be more homogenous due to the turbulent dispersion of droplets over the section of the channel. The experimental and numerical results agree starting from 120 mm, once the small droplets evaporated. Nevertheless, the numerical mean global temperature cannot be compared with the experimental data because the averaging technique is not the same in both experience and numerical simulation.

Figure 17 shows a typical image of the instantaneous n-octane vapor field. On the same image were plotted the droplets as they appear in the carrier flow. The visualization of the vapor field shows a great spatial heterogeneity in vapor concentration. It can be noted the existence of vapor clouds that alternate with regions with less density of vapors. The simultaneous presentation of gaseous and liquid phases allows concluding that droplets and vapor follow together the coherent structures of the turbulent flow. In addition, the shape of the vapor wake indicates the trajectory of the cloud of droplets.

Figure 18 shows radial profiles of mean n-octane vapor concentration at different distances from the injector. It is interesting to remark that the vapor concentration is higher near the channel wall. Investigating experimentally the vaporization of acetone in the same conditions as in the present study, M. Cochet [10] explained this behavior by the fact that droplets evaporate more rapidly as they impact the hot walls. Numerically, for the n-octane, we obtain the same behavior of the vapor field with no modeling of the droplet impact. It can be supposed that the droplet impinging the walls is not the single mechanism at the origin of this behavior, but the movement of turbulent structures in the channel also plays an important role. To emphasize this conclusion, during the numerical simulation it was observed a displacement of groups of droplets towards the channel walls. This displacement can be also at the origin of the dissymmetry in the mean vapor concentration profile. When the distance from the channel entrance increases the mean concentration profiles get more homogeneous due to the turbulent mixing.

Although the experimental level of turbulence cannot be achieved by the present simulation, the description of the dispersed phase seems consistent with the experimental data. A possible reason is that the influence of the mean convective flow plays a more important role than the turbulent fluctuations for the vaporization phenomenon.

Acknowledgement

The authors are grateful to the ASTRA program funded by CNRS and ONERA.

This research project has been supported by a Marie Curie Early Stage Research Training Fellowship of the European Community's Sixth Framework Programme under contract number MEST-CT-2005-020426. ""

Nomenclature

g	gravity acceleration [m/s ²]
v, U	velocity [m/s]
T_g	temperature [K]
c_{pl}	Specific heat capacity of the liquid [J/kg K]
r	Radius [m]
D	Diameter [m]
m	Mass [kg]
x	Coordinates [m]
L_v	Latent heat of vaporization [kJ/kg]
C_d	Drag coefficient
Nu	Nusselt number
Sc	Schmidt Number
Sh	Sherwood number
B_M	Mass Spalding number
B_T	Heat transfer Spalding number
Pr	Gas Prandtl number
Re	Reynolds Number
I	Turbulent intensity
H	Width of the channel cross-section [m]
ρ	Density [kg/m ³]
μ	Dynamic viscosity [Pa s]
λ	Thermal conductivity [W/mK]
τ	Dynamic relaxation time [s]

Subscripts

g	gas
p	droplet

References

- [1] Doué, N., "Modélisation de l'évaporation de gouttes multicomposants", Ph D Thesis, École Nationale Supérieure de l'Aéronautique et de l'Espace, 2005.
- [2] Laurent, C., "Amélioration et validation des modèles d'évaporation multi-composant", Ph D Thesis, ISAE 2008.
- [3] Bodoc, V., Wilms, J., Biscos, Y. and Lavergne, G., *ILASS 2008*, Como, Italy, September 2008;
- [4] Cochet, M., Ferret, B. and Bazile, R., *5th International Symposium on Turbulence, Heat and Mass Transfer (THMT)*, Dubrovnik, Croatia, September 2006
- [5] Bodoc, V., Moreau, F., Biscos, Y., Basile and R., Lavergne, G., *ICLASS 2009*, Vail, USA, July 2009
- [6] S. Saengkaew, "Study of spray heat up: On the development of global rainbow techniques", Ph.D. thesis, Rouen University, 2005
- [7] Özdemir, I. B. and Whitelaw, J. H., *Journal of Fluid Mechanics* 240: 503-532 (1992)
- [8] Xu, Hongyi., Khalid, Mahmood and Pollard, Andrew, *International Journal of Computational Fluid Dynamics* 17: 339-356, 2003
- [9] Chung, Y.M., Luo, K.H. and Sandham, N.D., *International Journal of Heat and Fluid Flow* 23: 592-600 (2002)
- [10] Cochet, M., Bazile, R., Ferret, B. and Cazin, S., *Experimental Fluids* 47:379-394 (2009)

Table 1. Operating conditions

Temperature of the air (at the nozzle position)	137 °C
Air bulk velocity	1 m/s
Liquid mass loading	8.7 %
Liquid flow rate	0.41 g/s
Temperature of the liquid	12 °C

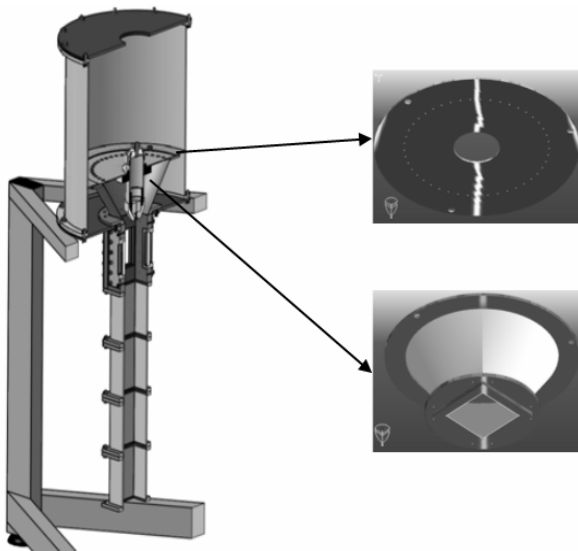


Figure 1. Experimental setup.

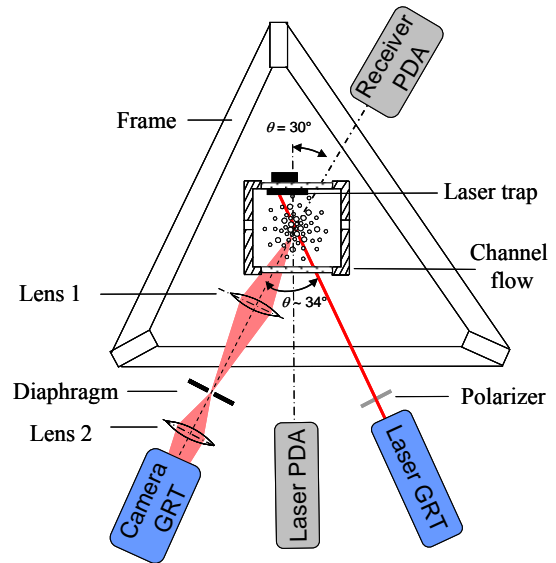


Figure 2. Schematic view through section.

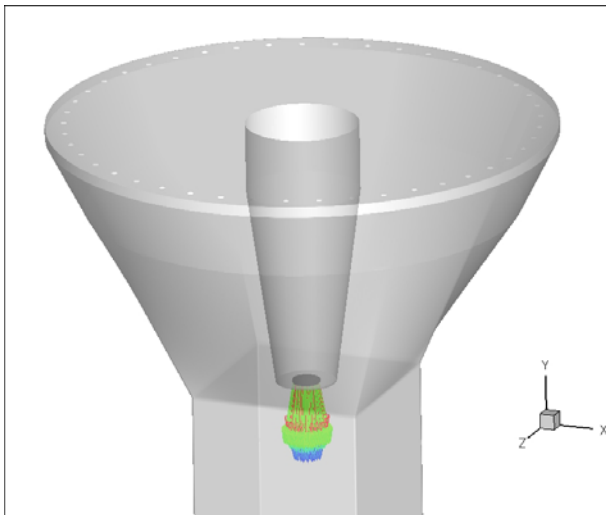


Figure 3. Geometry of the computing domain and the injection of droplets.

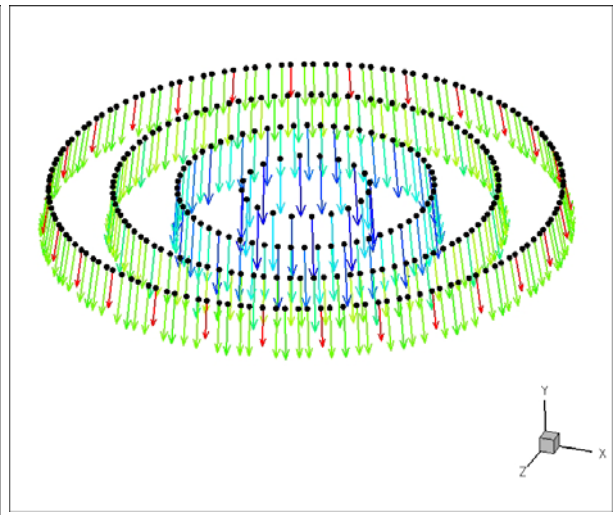


Figure 4. Example of injection points distribution and velocity vectors.

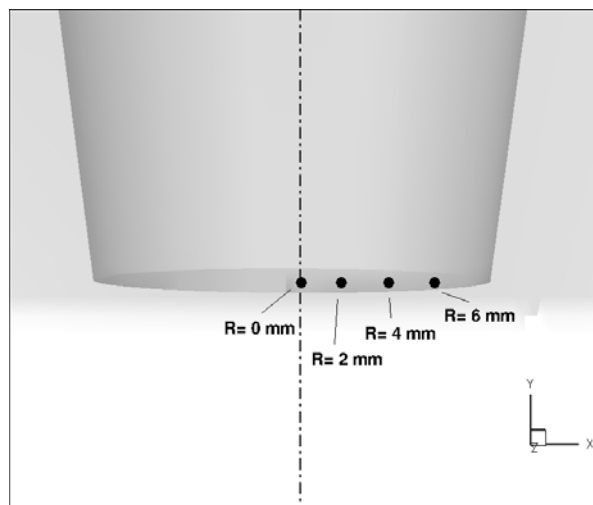


Figure 5. Radial PDA measurement positions.

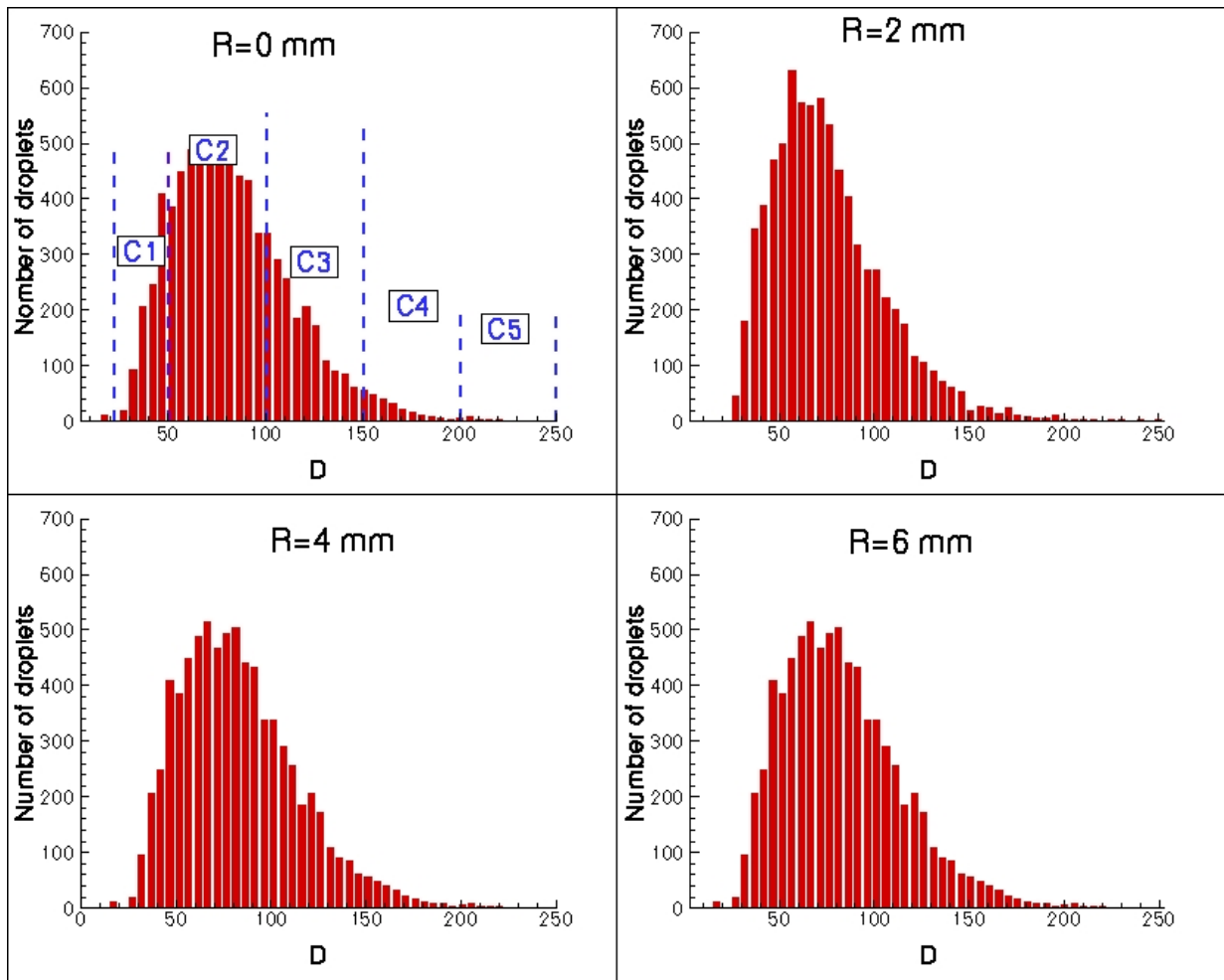


Figure 6. Experimental size histograms at different radial positions ($Y=10$ mm)

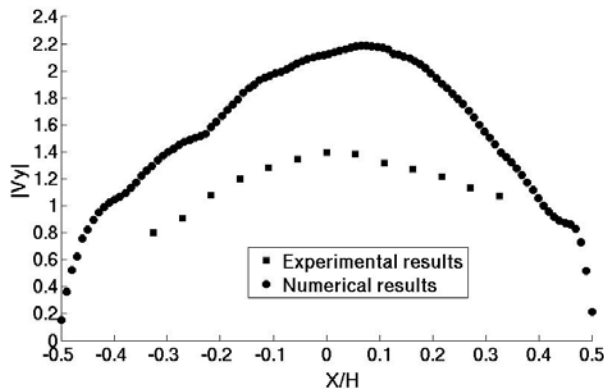


Figure 7. Radial evolution of the longitudinal mean velocity at 55 mm from the entrance in the channel.

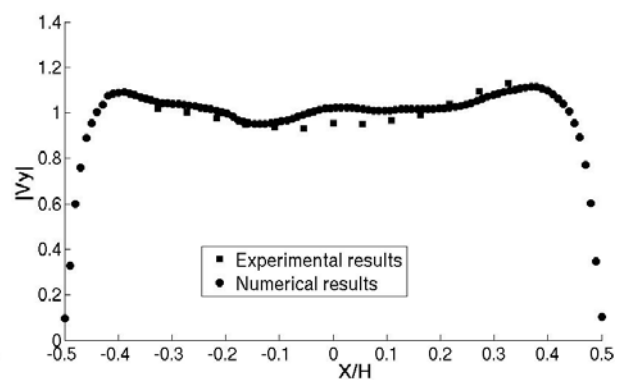


Figure 8. Radial evolution of the longitudinal mean velocity at 275 mm from the entrance in the channel

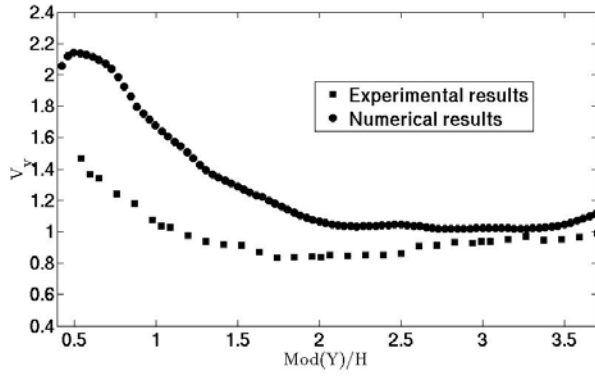


Figure 9. Axial evolution of the longitudinal mean velocity.

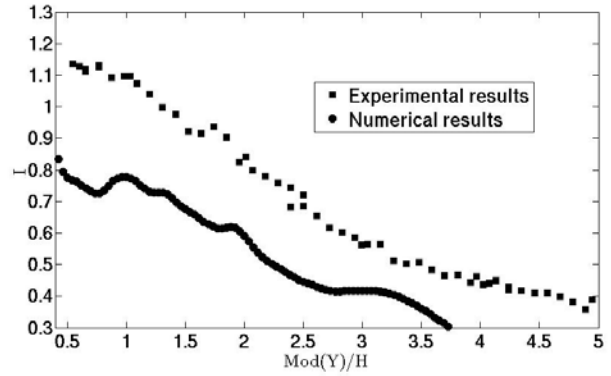


Figure 10. Axial evolution of the turbulent intensity.

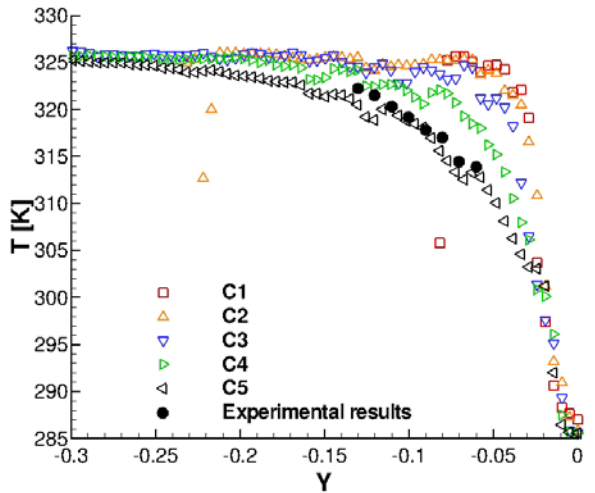


Figure 11. Axial evolution of the droplet temperature.

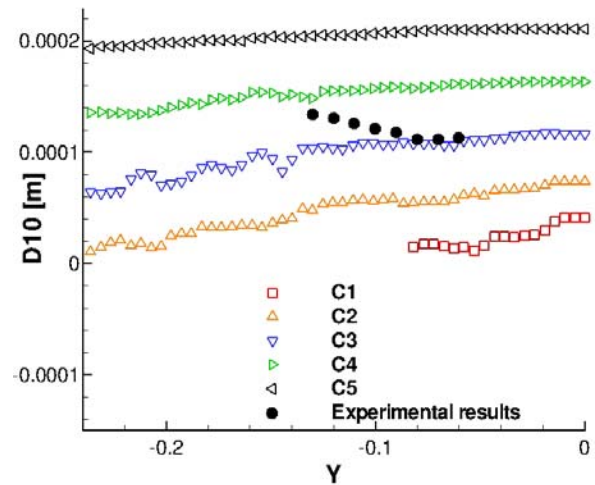


Figure 12. Axial evolution of the droplet mean size.

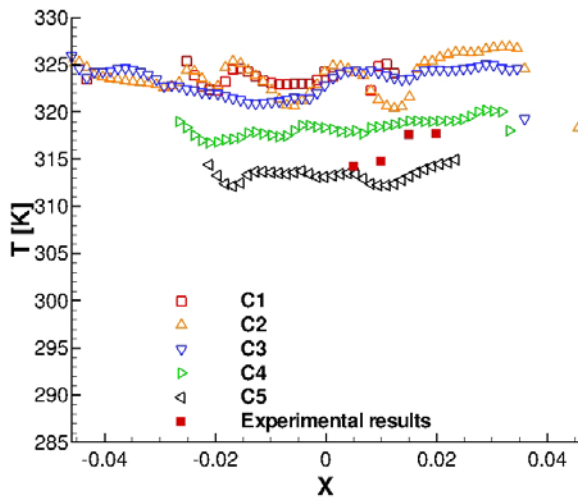


Figure 13. Radial evolution of the droplet temperature at 60 mm from the entrance in the channel.

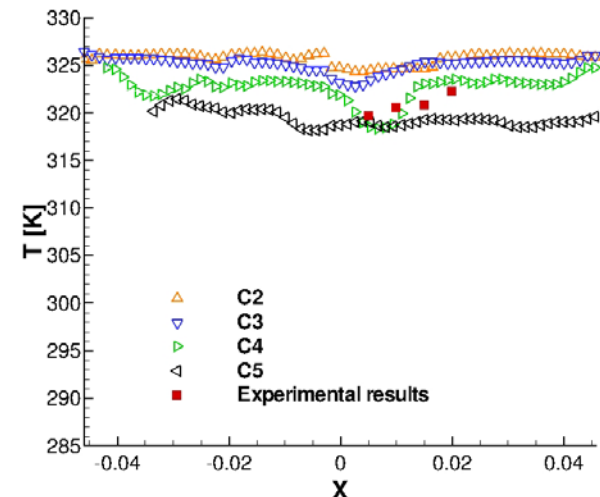


Figure 14. Radial evolution of the droplet temperature at 100 mm from the entrance in the channel.

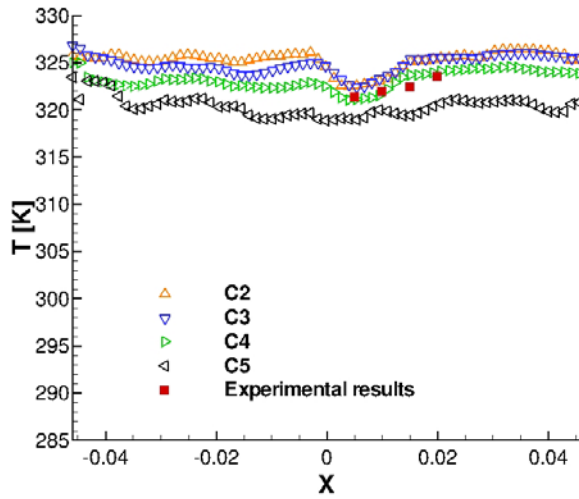


Figure 15. Radial evolution of the droplet temperature at 120 mm from the entrance in the channel.

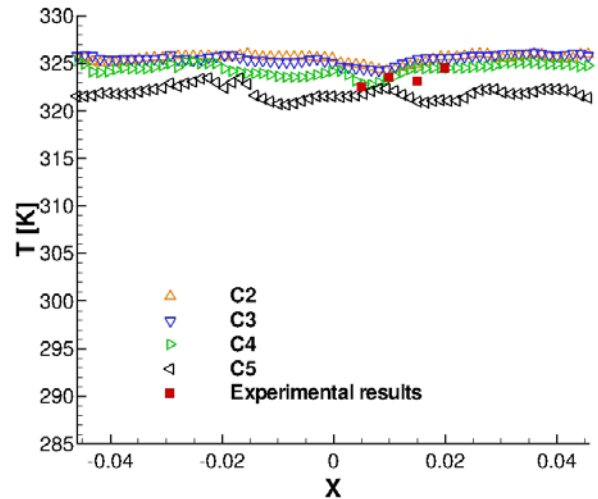


Figure 16. Radial evolution of the droplet temperature at 140 mm from the entrance in the channel.

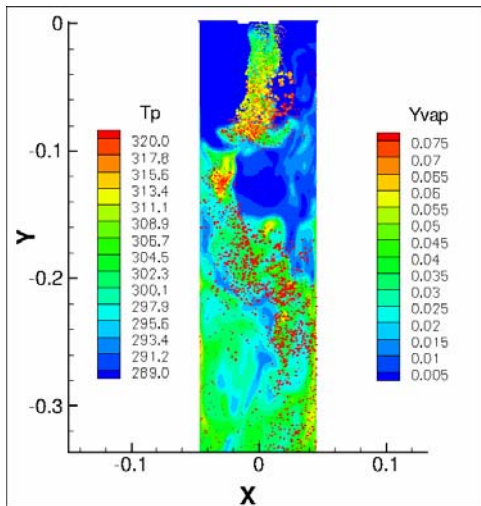


Figure 17. Instantaneous concentration field of n-octane vapour. Simultaneously, the numerical droplets are plotted.

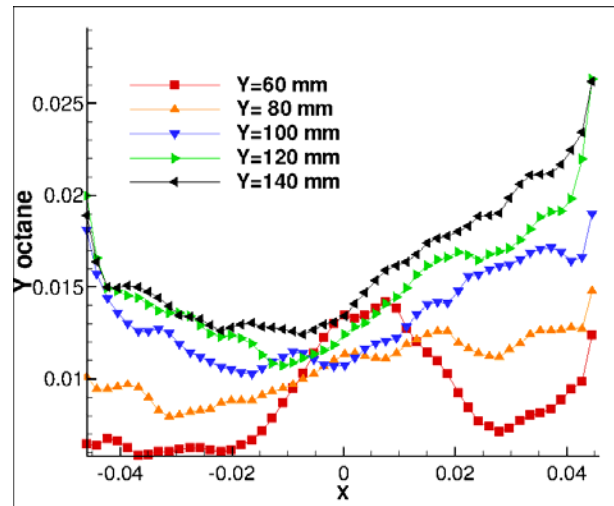


Figure 18. Radial profiles of mean vapour concentrations.